Minimal energy thresholds for sustained turbulent bands in channel flow

E. Parente[1,2,†], J.-Ch. Robinet[1], P. De Palma[2] and S. Cherubini[2]

[1]DynFluid - Arts et Métiers Paris, 151 Bd de l'Hôpital, 75013 Paris, France

[2]Dipartimento di Meccanica, Matematica e Management (DMMM), Politecnico di Bari, Via Re David 200, 70126 Bari, Italy

In this work, nonlinear variational optimization is used for obtaining minimal seeds for the formation of turbulent bands in channel flow. Using nonlinear optimization together with energy bisection, we have found that the minimal energy threshold for obtaining spatially patterned turbulence scales with $Re^{-8.5}$ for $Re > 1000$. The minimal seed, which is different to that found in a much smaller domain, is characterized by a spot-like structure surrounded by a low-amplitude large-scale quadrupolar flow filling the whole domain. This minimal-energy perturbation of the laminar flow has dominant wavelengths close to 4 in the streamwise direction and 1 in the spanwise direction, and is characterized by a spatial localization increasing with the Reynolds number. At $Re \lesssim 1200$, the minimal seed evolves in time, creating an isolated oblique band, whereas for $Re \gtrsim 1200$, a quasi-spanwise-symmetric evolution is observed, giving rise to two distinct bands. A similar evolution is found also at low Re for non-minimal optimal perturbations. This highlights two different mechanisms of formation of turbulent bands in channel flow, depending on the Reynolds number and initial energy of the perturbation. The selection of one of these two mechanisms appears to be dependent on the probability of decay of the newly created stripe, which increases with time, but decreases with the Reynolds number.

Key words: nonlinear instability, shear-flow instability, transition to turbulence

1. Introduction

Since the experimental work of Reynolds (1883), who firstly observed subcritical transition to turbulence in a wall-bounded shear flow, the dynamics of transition has remained an open problem of fluid dynamics. One of the most intriguing features of transitional flows is that turbulence does not arise at the same time in the whole domain, being preceded by the formation of localized flow structures that grow in amplitude and spread in space.

† Email address for correspondence: enzaparente@gmail.com

The first of these localized flow features to be observed were turbulent spots, which have been investigated by many researchers in the past. Emmons (1951) was the first to show experimentally, for a boundary-layer flow over a flat plate, that turbulent spots may trigger turbulence; later, this was confirmed experimentally and numerically in plane channel flow, analysing the spot characteristics (Carlson, Widnall & Peeters 1982; Henningson & Kim 1991; Klingmann 1992; Aida, Tsukahara & Kawaguchi 2010, 2011; Lemoult, Aider & Wesfreid 2013; Lemoult *et al.* 2014). In pipe flows, other localized flow structures – dubbed puffs – are observed both numerically and experimentally (Eckhardt *et al.* 2007; Avila *et al.* 2011). Puffs are localized, downstream-travelling flow structures within a laminar field, sustained by the energy provided by the neighbouring laminar motion at the upstream end of the puff. They can decay, split or merge, filling the laminar flow with turbulent fluctuations. More recently, Duguet, Schlatter & Henningson (2010) have shown that when locally perturbing the plane Couette flow, the fully turbulent state is preceded by the formation of turbulent bands. The same behaviour was reported by Tao & Xiong (2013) and Xiong *et al.* (2015), who have shown that after injecting a localized perturbation, turbulent bands grow obliquely in the domain until decay or breakdown to turbulence. In the latter case, it was assessed that the turbulent bands' lifetime is longer than that of turbulent spots. Besides having a crucial role in turbulent transition, oblique turbulent bands characterize also the (transient) turbulent state in shear flows at low Reynolds numbers, as shown by Tsukahara *et al.* (2005). In fact, in the pipe, plane Couette and plane Poiseuille flow, there is a range of moderate Reynolds numbers for which experiments and numerical simulations have shown that turbulence is not fully extended in space, since localized regions characterized by laminar and turbulent behaviour coexist when the statistically steady turbulent state is reached. Indeed, elongated oblique self-sustained turbulent bands within a laminar flow appear in plane Couette flow at $Re > 290$ (Prigent *et al.* 2002; Barkley & Tuckerman 2005; Duguet *et al.* 2010; Tuckerman & Barkley 2011), and in plane Poiseuille flow for $Re \geqslant 1000$ (Tsukahara, Kawaguchi & Kawamura 2014; Tuckerman *et al.* 2014; Tao, Eckhardt & Xiong 2018; Shimizu & Manneville 2019; Kashyap, Duguet & Dauchot 2020). In the channel flow, turbulent–laminar oblique patterns were observed experimentally for $Re = 1000$ by Carlson *et al.* (1982). Numerical simulations reproduced these patterns also at lower Reynolds numbers (Xiong *et al.* 2015; Tao & Xiong 2017; Kashyap *et al.* 2020), estimating a threshold value for observing turbulent bands at $Re \approx 660$, according to Tao *et al.* (2018). Recently, Gomé, Tuckerman & Barkley (2020) investigated the decay and splitting of these turbulent bands, finding that as the Reynolds number increases, their mean decay time increases and the mean splitting time decreases. At the 'critical' Reynolds number, estimated to be $\approx$965, these times are approximately equal. Thus it has been established that inclined bands persist for times of order $t \approx O(10^5–10^6)$ only when $Re > 965$, whereas they decay rapidly for lower values of Re. Song & Xiao (2020) reported recently the onset of such turbulent bands even at Reynolds number as low as $Re = 500$, generated by forcing the flow with a local perturbation with a sufficiently strong spanwise inflection. They showed that this forcing method permits us to generate bands at very low values of the Reynolds number, for which bands appeared previously to be not sustained. This procedure was motivated by the work of Xiao & Song (2020), where the authors performed a linear stability analysis of the mean velocity profile extracted in a small domain at the head of the turbulent band. By means of the stability analysis, it was suggested that spanwise inflectional instability may be the mechanism involved in the growth and self-sustaining process of turbulent bands.

In addition to the Reynolds number, the domain size plays an important role in the growth and self-interaction of turbulent bands. When the considered domain is sufficiently large, turbulent bands can grow for longer times, avoiding the probability of interaction with themselves or other bands. For this reason, several works studied the influence of the domain extension on the onset of turbulent bands. In order to reduce the computational cost, some numerical studies cleverly considered computational domains tilted in the direction of the bands, as done for plane Couette flow by Barkley & Tuckerman (2005) and for plane Poiseuille flow by Tuckerman *et al.* (2014). Very recently, Parente *et al.* (2021) carried out an optimal growth analysis in a tilted domain with given angle. They showed that although linear optimization is able to recover the main wavenumbers observed by direct numerical simulation, nonlinear effects are necessary for providing large-scale flow and spatial localization of the perturbation able to generate a turbulent band. Although very interesting for studying the dynamics of a single band, using the tilted domain constrains the turbulent bands to develop at a fixed angle and avoids (or reduces) the interactions with other bands, consequently resulting in a less rich dynamics. A more detailed analysis of laminar–turbulent patterns in shear flows is tackled in the review of Tuckerman, Chantry & Barkley (2020).

In the literature, typically two strategies are used to obtain turbulent bands. The first consists in starting from a space-filling statistically steady turbulent state, and slowly decreasing the Reynolds number until patterned laminar regions in the initially turbulent flow begin to appear (Tsukahara *et al.* 2005; Kashyap *et al.* 2020). This method usually leads to the formation of statistically steady laminar–turbulent patterns. Another method consists of perturbing the laminar flow with suitable localized disturbances having enough energy to trigger localized regions of turbulence eventually evolving into oblique stripes (Duguet *et al.* 2010; Aida *et al.* 2010, 2011; Tao & Xiong 2013; Xiong *et al.* 2015). When focusing on the second method, the amplitude, shape and localization of these initial perturbations should be chosen carefully to ensure their growth towards oblique bands. Depending on their shape, perturbations with higher amplitude may decay, while weaker perturbations may lead the flow to transition.

From a phase-space point of view, the problem of finding perturbations eventually generating these laminar–turbulent patterns consists of placing the starting point of the trajectory beyond the boundary of the basin of attraction of the laminar solution. Notably, the most relevant point of this boundary is its energy minimum, since it represents the minimal (in energy norm) perturbation of the laminar state that can lead the flow to transition. This point in the phase space has been dubbed, by Rabin, Caulfield & Kerswell (2012), 'minimal seed' for turbulent transition. This energy minimum has been assessed for several shear flows, aiming at finding minimal energy thresholds for transition. In particular, in plane Couette flows, a minimal energy threshold varying with the Reynolds number as $Re^{-2.7}$ has been found, in quantitative agreement with experimental estimates for pipe flows, whereas for the asymptotic-suction boundary layer, Cherubini, De Palma & Robinet (2015) found a scaling law of this energy threshold of Re^{-2}. Recently, Vavaliaris, Beneitez & Henningson (2020) performed similar computations for a non-parallel boundary-layer flow but did not provide a scaling law with respect to the Reynolds number. The determination of these energy thresholds is of primary importance for control purposes, since passive or active control methods such as boundary manipulation (Rabin, Caulfield & Kerswell 2014) or profile flattening (Marensi, Willis & Kerswell 2019) able to increase this minimal energy would render these flows less prone to transition. However, to the authors' knowledge, the minimal seed computation has never been carried out for the channel flow. In Farano *et al.* (2015, 2016), a nonlinear optimization in channel flow has been performed for rather small target times, but without any energy bisection, which is needed for the determination of minimal seeds. Moreover, all the minimal seed computations reported in the literature, except those performed by Pringle, Willis & Kerswell (2015) in a pipe flow, have been carried out in relatively small domains, hampering the development of laminar–turbulent patterns. In very large domains, where laminar–turbulent oblique bands exist, the minimal transition thresholds potentially can be different from those obtained in small domains. In fact, in small domains, the periodicity imposed in the streamwise and spanwise directions causes the interaction of the front of the perturbation with its tail already in the first phases of transition. Consequently, the kinetic energy of disturbances grows rapidly and suddenly saturates when turbulence fills the whole domain, whereas in large domains, the perturbations evolve freely for long times without interacting with themselves, so the development of disturbance appears to depart from that observed in smaller domains already at small times. As observed by several authors, the kinetic energy keeps growing for very long times, before saturating to a statistically steady value. Notably, in sufficiently large domains, localized perturbations often develop in an inclined direction with respect to the mean flow. Such a behaviour can be observed already at times comparable with the typical target times of minimal seed optimizations (i.e. $O(100)$). This difference in the dynamics of the perturbations depending on the domain size suggests that important differences can be found between minimal seeds computed in small and large domains, influencing the initial phases of formation of the band. Thus the analysis of these minimal perturbations and of their evolution towards oblique bands can potentially unveil the main mechanisms leading to the formation and sustainment of these laminar–turbulent patterns.

This work aims to find minimal seeds for the generation of turbulent bands in channel flow. The methodology to find these perturbations is based on the nonlinear variational optimization first used in the boundary-layer flow by Cherubini *et al.* (2010*a*, 2011) and in pipe flow by Pringle & Kerswell (2010) and Pringle, Willis & Kerswell (2012), and then coupled with energy bisection by Rabin *et al.* (2012) for the plane Couette flow and by other authors for other shear flows (Duguet *et al.* 2013; Cherubini *et al.* 2015; Vavaliaris *et al.* 2020). In all these studies, the kinetic energy was considered as the objective function of the optimization, and the optimal perturbations associated to the minimal input energy were localized spatially. Similar behaviour was found in Couette flow by Monokrousos *et al.* (2011), maximizing the time integral of the entropy production. A detailed review of these methods is reported by Kerswell, Pringle & Willis (2014) and by Kerswell (2018). In the present work, we carry out for the first time the computation of minimal seeds in channel flow for very large domains, allowing the creation of laminar–turbulent patterned final states such as oblique stripes. The perturbation kinetic energy is used as the objective function of the nonlinear optimization, which appears to be an appropriate choice since many literature studies report peaks of kinetic energy during the development of turbulent bands (Tao *et al.* 2018). The minimal seeds obtained using this optimize-and-bisect method are found to change with the Reynolds number, presenting a power-law scaling of the initial energy $E_{0_{min}} \propto Re^{-\gamma}$, with γ being approximately four times larger than the values reported in other shear flows in smaller domains. Moreover, two distinct mechanisms of creation of turbulent bands are observed and discussed in detail.

The paper is organized in the following way. In § 2, the methodology is presented. In § 3, the main results of the optimization are reported and the nonlinear evolution in time of the optimal perturbation is discussed. Finally, in § 4, conclusions are drawn.

2. Problem formulation

The considered flow is a plane channel flow at Reynolds number $Re = U_c H/\nu$, where U_c is the centreline velocity of the laminar Poiseuille flow, H is the half-width of the channel, and ν is the kinematic viscosity. The Reynolds number is varied by changing the pressure gradient, while the volume flux remains constant, with bulk velocity $U_b = 2/3$. The dynamics of this flow is studied by decomposing the instantaneous velocity field, $\boldsymbol{u} = [u, v, w]^{\mathrm{T}}$, into the laminar base flow $\boldsymbol{U} = [U(y), 0, 0]^{\mathrm{T}}$ and a perturbation $\boldsymbol{u}' = [u', v', w']^{\mathrm{T}}$. The dynamics of the perturbations of the laminar base flow is computed by solving the perturbative nonlinear incompressible Navier–Stokes equations:

$$\left.\begin{aligned} &\frac{\partial u_i'}{\partial x_i} = 0, \\ &\frac{\partial u_i'}{\partial t} + u_j' \frac{\partial u_i'}{\partial x_j} + u_j' \frac{\partial U_i}{\partial x_j} + U_j \frac{\partial u_i'}{\partial x_j} = -\frac{\partial p'}{\partial x_i} + \frac{1}{Re} \frac{\partial^2 u_i'}{\partial x_j^2}, \end{aligned}\right\} \tag{2.1}$$

where $\boldsymbol{U} = [U(y), 0, 0]^{\mathrm{T}}$, $U(y) = 1 - y^2$, is the laminar streamwise velocity profile, p' is the pressure perturbation, and x_i is the Cartesian reference frame having components x, y, z, for the streamwise, wall-normal and spanwise directions, respectively. No-slip boundary conditions are imposed at the walls for the three velocity components, while periodicity is fixed in the streamwise and spanwise directions.

In order to find the minimal seed for the considered flow, we first search for the optimal perturbation $\boldsymbol{u}'$ at $t = 0$, providing the maximum value of the objective function at target time T. Following previous works (Cherubini *et al.* 2010*a*; Pringle & Kerswell 2010), we choose as objective function the energy gain $G(T) = E(T)/E(0)$, where

$$E(t) = \frac{1}{2V} \int_V (u'(t)^2 + v'(t)^2 + w'(t)^2)\, \mathrm{d}V \tag{2.2}$$

is the kinetic energy at time t, and V is the volume of the computational domain. In order to find the initial perturbation $\boldsymbol{u}'(0)$ having given initial energy $E(0) = E_0$, providing the largest possible energy $E(T)$ at the target time, an optimization loop is set using the Lagrange multiplier technique (Zuccher, Luchini & Bottaro 2004; Pringle & Kerswell 2010; Cherubini *et al.* 2011). A Lagrangian functional is defined by augmenting the objective function with the following constraints: (i) the optimal perturbation $\boldsymbol{u}'(t)$ must be a solution of the Navier–Stokes equations at all times $t \in [0, T]$; (ii) it must be divergence-free at all times $t \in [0, T]$; and (iii) it must have energy norm equal to a given value E_0 at $t = 0$. With these constraints, the Lagrangian functional reads

$$\begin{aligned} &\mathcal{L}(u_k', p', u_k^\dagger, p^\dagger, u_k'(0), u_k'(T), \lambda) \\ &\quad = \frac{E(T)}{E(0)} - \int_0^T \int_V u_i^\dagger \left(\frac{\partial u_i'}{\partial t} + \frac{\partial (u_i' u_j')}{\partial x_j} + \frac{\partial (U_i u_j')}{\partial x_j} + \frac{\partial (u_i' U_j)}{\partial x_j} + \frac{\partial p}{\partial x_i} - \frac{1}{Re} \frac{\partial^2 u_i'}{\partial x_j^2} \right) \mathrm{d}V\, \mathrm{d}t \\ &\qquad - \int_0^T \int_V p^\dagger \frac{\partial u_i'}{\partial x_i}\, \mathrm{d}V\, \mathrm{d}t - E^\dagger \left(\frac{E_0}{E(0)} - 1 \right), \end{aligned} \tag{2.3}$$

with $\boldsymbol{u}^\dagger$, $p^\dagger$ and $E^\dagger$ being the Lagrangian multipliers (or adjoint variables).

To maximize the augmented functional $\mathcal{L}$, we evaluate its variation with respect to the direct and adjoint variables, and nullify it. The variation of the Lagrangian functional with respect to the direct variables $\boldsymbol{u}'$, p' provides the adjoint equations

$$\left.\begin{aligned} &\frac{\partial u_i^\dagger}{\partial x_i} = 0, \\ &\frac{\partial u_i^\dagger}{\partial t} - u_j^\dagger \frac{\partial u_i'}{\partial x_j} + u_j' \frac{\partial u_i^\dagger}{\partial x_j} - u_j^\dagger \frac{\partial U_i}{\partial x_j} + U_j \frac{\partial u_i^\dagger}{\partial x_j} = -\frac{\partial p^\dagger}{\partial x_i} - \frac{1}{Re} \frac{\partial^2 u_i^\dagger}{\partial x_j^2}. \end{aligned}\right\} \tag{2.4}$$

The optimization problem is then solved using a direct–adjoint looping algorithm (as done by Pringle & Kerswell (2010) and Cherubini *et al.* (2010*a*), among others), which consists in integrating iteratively in time the direct and adjoint equations between 0 and T to evaluate the gradient of $\mathcal{L}$ with respect to $\boldsymbol{u}'(0)$, which is then used to update the initial perturbation using a gradient rotation algorithm (Foures, Caulfield & Schmid 2013; Farano *et al.* 2016, 2017). Convergence is attained when the variation of the gain between two successively iterations is smaller then a chosen threshold $\epsilon = 5 \times 10^{-8}$.

For computing the minimal seed, the variational optimization is coupled with an energy-bisection procedure. Two different optimizations are initialized with a random divergence-free perturbation for low T, with a value of E_0 sufficiently high (low) to induce transition (relaminarization) at longer times. The energy is bisected and the optimization repeated, using the results of the previous optimization as initial guess. Energy bisection is carried out at first for a low ($O(10)$) target time in order to have a very rough (but computationally cheap) upper estimate of the initial minimal energy threshold $E_{0_{min}}$. Then the target time is increased at $O(100)$ and the energy bisection is repeated, allowing the result to converge towards $E_{0_{min}}$.

The optimization algorithm is implemented within the open source code Channelflow (channelflow.ch; Gibson *et al.* 2021). Both direct and adjoint equations are solved using a Fourier–Chebyshev discretization in space and a third-order semi-implicit backward difference scheme for the time integration. An influence matrix method with Chebyshev tau correction was used to enforce the no-slip boundary condition at the walls.

The domain size in the streamwise, normal and spanwise directions is $L_x \times L_y \times L_z = 250 \times 2 \times 125$, while the number of grid points in the same directions are $N_x \times N_y \times N_z = 1024 \times 65 \times 1024$. This results in a numerical resolution comparable with the values used by Shimizu & Manneville (2019) and Kashyap *et al.* (2020) for the same range of Reynolds numbers. Finally, it should be noticed that the fact that optimizations are performed in a large domain involves challenging computations in terms of memory, especially for the highest considered target time, $T = 150$. In fact, the direct–adjoint algorithm requires storage of the flow field snapshots $\boldsymbol{u}'$ at each time step, in order to evaluate the term coupling direct and adjoint variables in the adjoint equations. To alleviate the storage requirement, a checkpointing technique is used, similar to that used in Griewank & Walther (2000) and Hinze, Walther & Sternberg (2006).

3. Results

Nonlinear optimizations are performed for four values of the Reynolds number, $Re = 1000$, 1150, 1250, 1568, chosen in the range of Reynolds numbers for which the plane Poiseuille flow is linearly stable and the turbulent state appears in the form of persistent turbulent–laminar patterns (Tao *et al.* 2018; Gomé *et al.* 2020; Kashyap *et al.* 2020). As reported by Xiong *et al.* (2015) and Gomé *et al.* (2020), the onset of bands does not lead to sustained turbulence for $Re \lesssim 1000$, whereas for $Re \gtrsim 1000$, the bands can split, providing a mechanism for turbulence spreading, leading to the coexistence of laminar regions with inclined turbulent bands, which persist up to $Re > 3900$, for which only featureless turbulence is present. Figure 1(*a*) provides the influence of the target time on the optimal energy gain for $Re = 1150$ and given input energy $E_0 = 1.1 \times 10^{-7}$. The energy gain grows with the target time following a quasi-exponential trend for $T < 40$ and $T > 50$, reaching an amplification of three orders of magnitude for $T > 80$. No saturation of the final energy is observed for $T \leqslant 100$, since very long (i.e. $O(10^3)$) times would be needed to fill the entire domain with turbulent bands, as will be shown in § 3.3. As mentioned before, the procedure of bisection of the initial energy is carried out at first for $T = 10$, in order to have a computationally cheap upper bound for the computation of E_{0min}, which will be then carried out for $T = 100$ or $T = 150$, depending on the Reynolds number. For $Re < 1568$, the estimate of E_{0min} was obtained for $T = 100$, since we have verified that increasing the target time from $T = 100$ to $T = 150$ leads to slight changes of the minimal energy, namely, from 5.6×10^{-7} to 5.5×10^{-7} for $Re = 1000$. But at $Re = 1568$, it has been necessary to increase the target time to $T = 150$ to achieve a sufficiently good approximation of the threshold energy for generating bands. Figure 1(*b*) provides the minimal input energy able to induce transition towards the turbulent bands, E_{0min} (red dots), together with its upper estimate obtained for $T = 10$ (black dots), for the four considered values of the Reynolds number. In the range of Re analysed, we tried to fit the minimal input energy with a power law of the type $E_{0_{min}} \propto Re^{-\gamma}$, but we obtained a satisfactory fit only by restraining the power law to the minimal seeds in the range $Re > 1000$, represented by the red dashed line corresponding to $\gamma \approx 8.5$. A similar behaviour is observed for the upper estimate of $E_{0_{min}}$ obtained for $T = 10$ (black dots), although the associated value of γ is much lower. Incidentally, we observe that as expected, larger threshold initial energies are obtained for the lower target time $T = 10$ (black line). The fact that the minimal seed energy obtained for $Re = 1000$ appears not to be aligned with the fitting line recovered for larger values of Re might have been anticipated. As reported by Xiong *et al.* (2015), $Re = 1000$ is very close to the limit value of the Reynolds number for which band splitting begins to be observed. Thus at this threshold value of Re, the flow dynamics may present a transitional behaviour between two different regimes, not fitting with that observed at larger values of Re. Finally, it is also worth noticing that the exponent of the power law approximating the minimal-energy threshold is much higher than values reported in previous works. For the plane Couette flow, a minimal seed energy varying as $Re^{-2.7}$ was reported by Duguet *et al.* (2013); for the asymptotic suction boundary layer, a scaling of Re^{-2} was found by Cherubini *et al.* (2015). This difference might be linked to either the much larger domain considered in the present study, or the different type of flow.

To investigate this interesting point, we have performed minimal seed computations in a much smaller domain with size $L_x \times L_y \times L_z = 2\pi \times 2 \times \pi$. Unfortunately, we have found that for $Re < 1400$, turbulence does not remain self-sustained for a sufficiently long time to allow convergence of the algorithm. Thus we have computed the minimal energy thresholds for a rather different set of Reynolds numbers, namely, $Re = 1400, 1568, 1650$. As shown by the blue symbols in figure 1(*b*), we have found that the minimal energy thresholds for transition to turbulence in the smaller domain are several orders of magnitude larger than those found previously for the larger domain. In particular, for $Re = 1568$, the minimal energy for transition is $E_{0min} = 7.1 \times 10^{-6}$ in the small domain, three orders of magnitude larger than the value obtained for the large domain, namely, $E_{0min} = 3.6 \times 10^{-9}$. This might have been anticipated, since E has been defined as an energy density, thus is normalized by the volume of the computational domain.

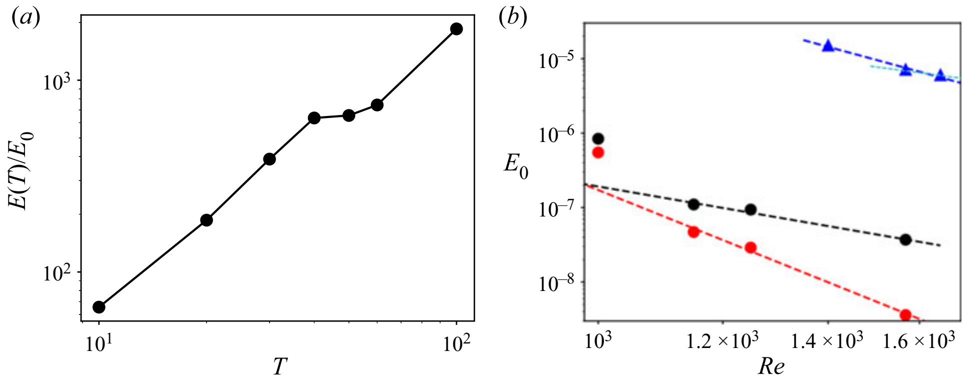

Figure 1. (*a*) Optimal energy gain versus target time T for $Re = 1150$ and $E_0 = 1.1 \times 10^{-7}$. (*b*) Minimal energy threshold E_{0min} for transition to turbulence (red dots) and upper estimate obtained for $T = 10$ (black dots) in the large domain. The blue symbols refer to the minimal energy thresholds recovered in the small domain. The black and red lines represent the power laws for low ($O(10)$) and high ($O(100)$) target times, respectively, for the large domain at $Re > 1000$. The blue and cyan lines represent the power laws for the small domain at $Re \geqslant 1400$ and $Re \geqslant 1568$, respectively.

However, reporting the small-domain minimal energy estimate in the larger domain provides $E_{0min} = E_{0min}^{small} V^{small}/V^{large} = 4 \times 10^{-9}$, which is indeed larger than the large-domain estimate. Moreover, we have found that the scaling law of the minimal energy for the small-domain case is very close to that found for the large domain, at least in the considered range of Re. This may suggest that the higher value of the power-law exponent found in the present case, with respect to other flow cases, is due to the different type of flow, not to the domain size. However, we should mention that if we restrain the considered Reynolds number range to the two largest values (cyan dashed line), then the exponent of the scaling law drops to -3.3, a value that is closer to that of other shear flows, and to the value reported recently by private communication for the channel flow at higher values of Re (R. Kerswell, private communication). This might indicate that, similarly to what we have reported for the large domain, very close to the threshold Reynolds number for which turbulence is sustained, the minimal energy for transition strongly increases, departing from the scaling law recovered at higher values of Re. This could be verified only by performing minimal seed computations at higher Reynolds numbers, which is far from the scope of the present paper. Thus we can conclude that the scaling law appears mostly independent of the domain at very low values of Re, although it may differ strongly at higher Re. The domain size affects considerably the values of the minimal energy, as well as the shape and amplitudes of the minimal seeds, as will be shown in the next subsection.

3.1. *Nonlinear optimal perturbations*

The initial optimal solutions obtained for the target time $T = 10$ at the threshold energy able to trigger turbulence are shown in figure 2 for $Re = 1150$. The optimal perturbation is localized spatially in a small region of the domain, with a shape similar to that of a spot, being composed of alternating positive and negative finite-size streamwise streaks. Despite spatial localization having been observed already in nonlinear optimizations (for instance, see Cherubini *et al.* 2011; Monokrousos *et al.* 2011; Pringle *et al.* 2012), the structure of this optimal perturbation is rather different from that of previously computed nonlinear optimal perturbations, and more closely resembles the optimal wavepacket recovered by

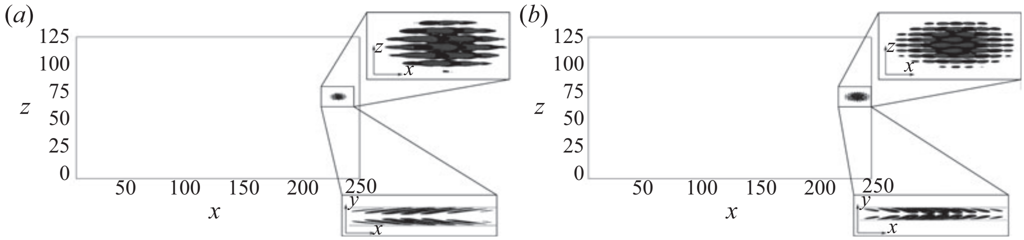

Figure 2. Nonlinear optimal perturbation at times $t = 0$ (*a*) and $t = T = 10$ (*b*), for $Re = 1150$ with the input energy $E_0 = 1.1 \times 10^{-7}$ (black dot in figure 1). The insets show isosurfaces of the streamwise velocity, light grey for positive and black for negative values, $u = \pm 0.003$ (top) and $u = \pm 0.02$ (bottom).

linear optimization and windowing, obtained for the boundary-layer flow by Cherubini *et al.* (2010*b*). This is probably due to the low target time and initial energy used for these computations, which hinders partially the development of nonlinear effects. At $t = 0$, the optimal perturbation presents vortical structures inclined in the opposite direction with respect to the shear, which reverse their inclination at target time (see the x–y planes in the bottom right of figures 2*a*,*b*). This streamwise tilting is a common feature of optimal perturbations in shear flows (Cherubini *et al.* 2010*a*; Pringle & Kerswell 2010; Duguet *et al.* 2013), and indicates that the Orr mechanism is a fundamental mechanism involved in the early stage of transition to turbulence, with characteristic time approximately equal to 10 (Orr 1907). Indeed, although it may seem unrealistic that perturbations inclined opposed to the mean flow can actually be observed in experiments and simulations of wall-bounded turbulent flows, recent works (Jiménez 2013) have argued that such types of disturbances are in fact created in the near-wall cycle during the streak breakdown.

Duguet & Schlatter (2013) show that oblique bands arise as a result of advection of newly nucleated streaks in the direction of a large-scale flow, which is oblique with respect to the streamwise direction. The local orientation of the large-scale flow is thus responsible for the obliqueness of the laminar–turbulent interface of growing incipient spots as well as for maintaining turbulent stripes (Duguet & Schlatter 2013). To ascertain whether the computed nonlinear optimal perturbations contain the seed for the development of turbulent bands, we compute the large-scale flow related to the optimal disturbances by averaging the instantaneous velocity field in the wall-normal direction as $\overline{u_i} = \int_{-1}^{1} u_i \, \mathrm{d}y$. Notice that $\bar{u}$ is zero where the flow is laminar, close to zero where the flow is turbulent, but non-zero at the laminar–turbulent interfaces, due to a mismatch of the streamwise flow rates across them, linked to the presence of overhang regions (Duguet & Schlatter 2013). Figure 3 provides the isocontours of the crossflow energy $E_{cf} = (1/2) \int (v^2 + w^2) \, \mathrm{d}y$, surrounded by the large-scale field $(\bar{u}, \bar{w})$, for the initial optimal perturbation at $Re = 1150$, $E_0 = 1.1 \times 10^{-7}$. The optimal flow field is characterized by two different scales: a small-scale flow embedded within the spot-like structure, and a large-scale flow in the form of large vortices filling the whole domain. The latter is characterized by a streamwise flow entering the spot and a spanwise flow exiting from it, constituting a quadrupolar structure. A quadrupolar large-scale flow around spots or turbulent bands has been observed in plane Couette flow (Schumacher & Eckhardt 2001; Lagha & Manneville 2007) and plane Poiseuille flow (Lemoult *et al.* 2014), and very recently in the Couette–Poiseuille flow (Klotz, Pavlenko & Wesfreid 2021). This large-scale structure appears within the flow due to the shearing of the streamwise velocity and the breaking of the spanwise homogeneity (Wang *et al.* 2020). Notice that this large-scale flow, which is not associated with the

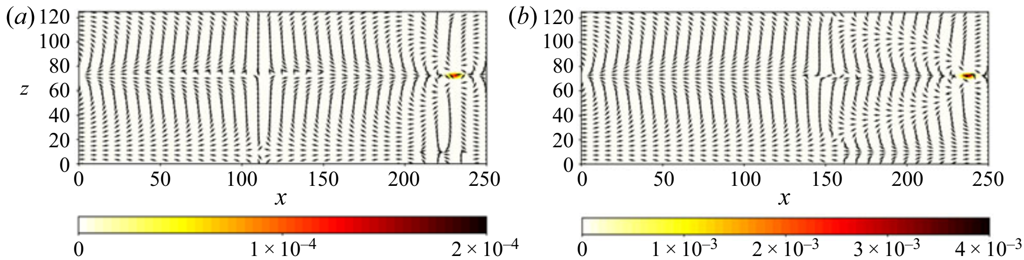

Figure 3. Shaded isocontours of the crossflow energy E_{cf} together with the normalized y-integrated large-scale flow (vectors) characterizing the nonlinear optimal perturbations for $Re = 1150$, $E_0 = 1.1 \times 10^{-7}$, $T = 10$: (*a*) initial optimal solution, $t = 0$; (*b*) optimal solution at the target time, $t = T$.

presence of overhang regions, remains almost unchanged from $t = 0$ to $t = T$ (compare figures 3*a*,*b*).

Increasing the target time to $T = 100$ for $Re = 1150$, while keeping $E_0 = 1.1 \times 10^{-7}$, we obtain a similar optimal structure, characterized by a quadrupolar large-scale flow surrounding a spot-like small-scale disturbances (not shown). Starting from this optimal (but yet not minimal) solution, the optimize-and-bisect procedure is carried out with $T = 100$ for $Re = 1150$. The same procedure is carried out for all the considered values of Re, for obtaining the minimal seeds whose energy is reported in figure 1(*b*).

3.2. *Minimal seed at different Reynolds numbers*

The minimal seeds for turbulent bands obtained for all the considered values of the Reynolds number are provided in figures 4 and 5 in two different views showing the streamwise and spanwise alternation of finite-size streaks together with spanwise-inclined vortical structures closer to the wall. Moreover, the large-scale flow, shown in figure 6 for $Re = 1150$, maintains the previously observed quadrupolar structure, presenting large-scale vortices quasi-symmetric in the spanwise direction. The same large-scale quadrupolar structure surrounding the minimal-energy wavepacket is observed also for the other considered Reynolds numbers (not shown). Quadrupolar structures similar to those observed around these optimal perturbations have been observed in several shear flows and spatial domains, in experiments and computations (see, for instance, Lundbladh & Johansson 1991; Lagha & Manneville 2007; Duguet & Schlatter 2013; Lemoult *et al.* 2013; Couliou & Monchaux 2015; Chantry, Tuckerman & Barkley 2016). This two-dimensional large-scale flow surrounding localized perturbations or turbulent spots, appears to fill out the whole domain, and shows an exponential (or algebraic) decay of its amplitude in space (see Schumacher & Eckhardt 2001; Brand & Gibson 2014). In particular, Wang *et al.* (2020) demonstrated that this quadrupolar structure is a generic feature of planar shear flows confined between two walls, and stems from (i) the shearing of the streamwise velocity, and (ii) the breaking of the spanwise homogeneity. The minimal seeds (and nonlinear optima) computed for all the considered Reynolds numbers show both these features, justifying the presence of these large-scale vortices. However, the small-scale minimal perturbations are found to change considerably with the Reynolds numbers, as shown in figure 4. In particular, a further localization of the initial wavepacket is observed for increasing Re, leading to a minimal structure at $Re = 1568$ localized on only one of the two walls (see figure 4*d*), which resembles closely that found for the plane Couette and the asymptotic suction boundary-layer flow in small domains (Rabin *et al.*

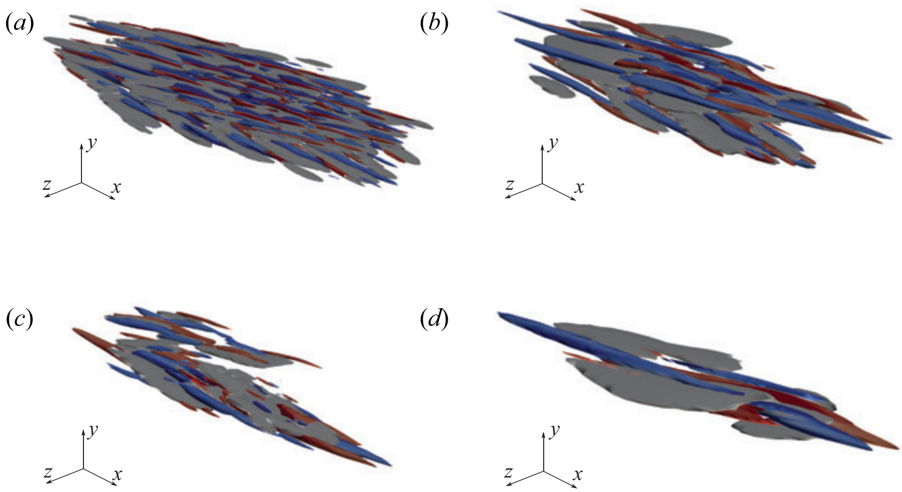

Figure 4. Minimal seeds at different Reynolds numbers: isosurfaces of negative streamwise velocity ($u = -0.0025$, light grey) and Q-criterion ($Q = 0.003$) coloured by the streamwise vorticity (positive red, negative blue). For all values of Re, only a subdomain of length $l_x \times l_y \times l_z = 16 \times 0.5 \times 6$ is shown. Here: (*a*) $Re = 1000$, $E_0 = 5.5 \times 10^{-7}$; (*b*) $Re = 1150$, $E_0 = 4.7 \times 10^{-8}$; (*c*) $Re = 1250$, $E_0 = 2.9 \times 10^{-8}$; (*d*) $Re = 1568$, $E_0 = 3.6 \times 10^{-9}$.

2012; Duguet *et al.* 2013; Cherubini *et al.* 2015). Apart from the spatial localization, the main structures observed within the minimal seed wavepackets are essentially the same, namely, finite-size streaks flanking upstream-tilted elongated vortices. As a result of the discrepancies recovered at initial time, the minimal seeds obtained at different Re evolve differently in time, presenting an increasing localization for larger values of Re, as provided in figures 7 and 8. However, all of the wavepackets present an arrow-shaped structure, with the downstream region essentially characterized by low-speed streaks, and the core region filled with small-scale vortices together with some coherent streamwise streaks. Despite having some common features with turbulent spots observed typically in transitional flows (Marxen & Zaki 2019), these perturbations at target time are characterized by more coherent streaks and vortices at their head, tail and sides, and a core showing signs of streak breakdown. Moreover, the large-scale quadrupolar structure observed at $t = 0$ is maintained at target time for all the considered values of Re, as shown in figure 6(*b*) for $Re = 1150$.

It is also interesting to compare such minimal seeds with those obtained in the previously mentioned smaller domain. A three-dimensional visualization of the small-domain minimal seeds is provided in figure 9 for the three considered Reynolds numbers. The streamwise perturbation patches alternating in the x and z directions are rather similar to those found for the large domain, although in the latter case this alternating structure is repeated many times in all spatial directions. Moreover, the amplitude of the small-domain minimal seeds is about twice that of the minimal perturbations obtained for the large domain, indicating that the size of the domain has a non-negligible effect on the shape, amplitude and energy of the minimal seeds. Finally, the isocontours of the crossflow energy surrounded by the large-scale field are shown in figure 10 for the small-domain minimal seeds. One can observe that a quadrupolar structure is present as well, but at a much smaller scale than in the previous case.

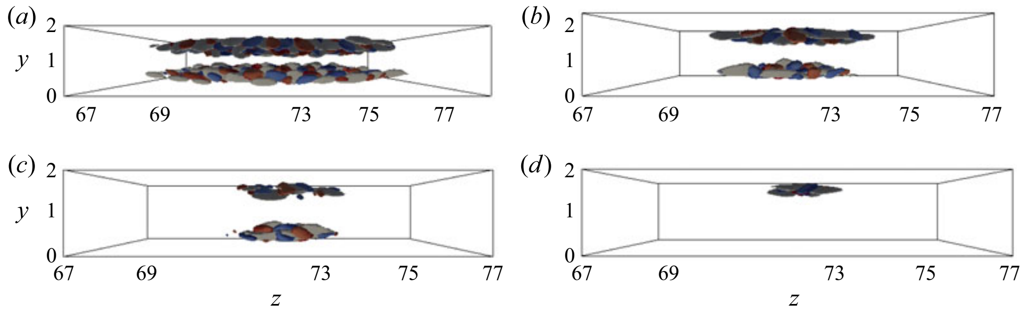

Figure 5. Minimal seeds at different Reynolds numbers: isosurfaces of negative streamwise velocity ($u = -0.0025$, light grey) and Q-criterion ($Q = 0.003$) coloured by the streamwise vorticity (positive red, negative blue). Here: (*a*) $Re = 1000$, $E_0 = 5.5 \times 10^{-7}$; (*b*) $Re = 1150$, $E_0 = 4.7 \times 10^{-8}$; (*c*) $Re = 1250$, $E_0 = 2.9 \times 10^{-8}$; (*d*) $Re = 1568$, $E_0 = 3.6 \times 10^{-9}$.

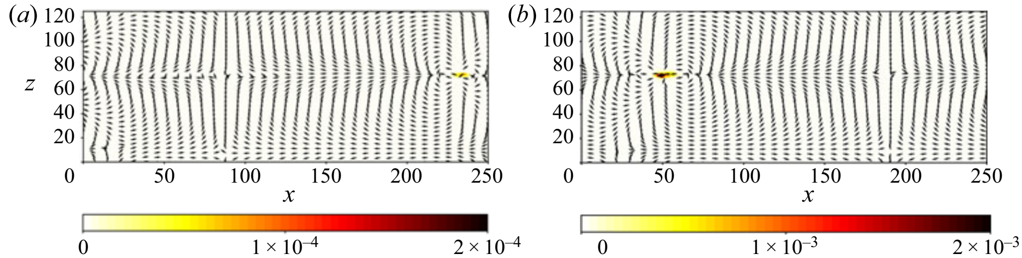

Figure 6. Isocontours of the crossflow energy E_{cf} with the normalized y-integrated large-scale flow (vectors) for $Re = 1150$, $E_0 = 4.7 \times 10^{-8}$, $T = 100$: (*a*) initial optimal solution, $t = 0$; (*b*) optimal solution at the target time, $t = T$.

The contours of the premultiplied energy spectra of the minimal seed obtained at $Re = 1150$ are reported in figure 11. The streamwise perturbation energy peaks for $\lambda_z \approx 2.45$ and $\lambda_x \approx 3.78$ (see also table 1), whereas the wall-normal and spanwise perturbation energy have largest amplitude at $\lambda_z \approx 1$, $\lambda_x \approx 4$, with a secondary peak for $\lambda_z \approx 2$ and $\lambda_x \approx 25$. The lowest of these wavelengths are close to those reported by Lemoult *et al.* (2014) concerning the development of turbulent spots at similar Reynolds numbers, and are linked to the finite size of the streaks, whereas the largest wavelengths are linked directly to the streamwise and spanwise sizes of the wavepacket. Very similar spectra are found to characterize the nonlinear optimal perturbations at higher initial energy (solid contours in figure 11). The premultiplied energy spectra of the minimal seeds obtained for the other values of Re are reported in figure 12 by the shaded contours ($Re = 1000$) and the dashed lines (black for $Re = 1150$, blue for $Re = 1250$, green for $Re = 1568$). As a consequence of the increased spatial localization, the overall distribution of the energy spectra is displaced towards higher values of λ_x, λ_z when Re increases. This effect is coupled with a narrowing and displacement of the spectra towards higher values of y, which is a consequence of an increased localization also in the wall-normal direction. The peak values reported in table 1 are also influenced considerably by the Reynolds number.

3.3. *Minimal seed evolution in time*

In this subsection, we analyse the time evolution of the minimal seeds towards the turbulent bands. In figure 13, the time evolution of the kinetic energy, obtained from direct numerical

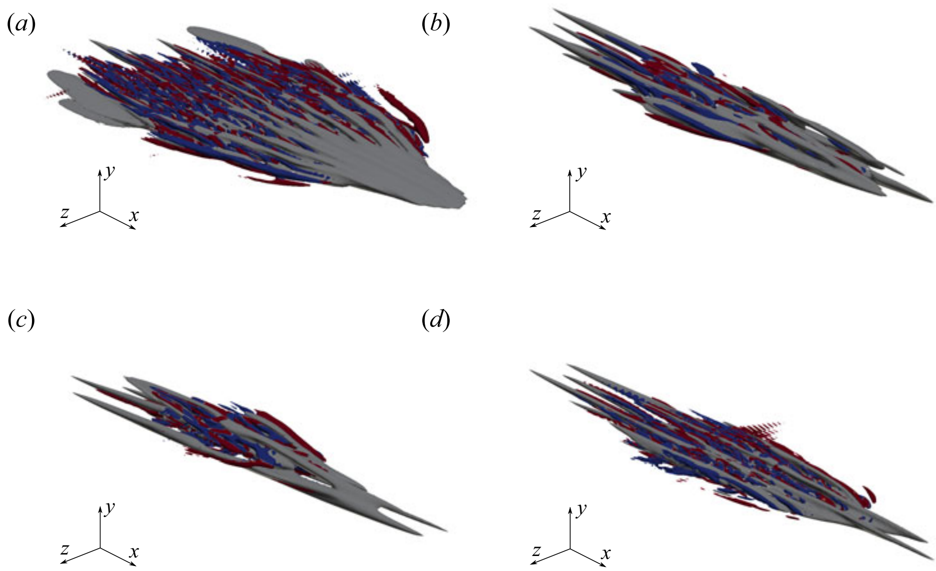

Figure 7. Minimal seeds at target time $t = T$ for different Reynolds numbers: isosurfaces of negative streamwise velocity ($u = -0.03$, light grey) and Q-criterion ($Q = 0.005$) coloured by the streamwise vorticity (positive red, negative blue). For all values of Re, only a subdomain of length $l_x \times l_y \times l_z = 30 \times 0.5 \times 10$ is shown. Here: (*a*) $Re = 1000$, $E_0 = 5.5 \times 10^{-7}$; (*b*) $Re = 1150$, $E_0 = 4.7 \times 10^{-8}$; (*c*) $Re = 1250$, $E_0 = 2.9 \times 10^{-8}$; (*d*) $Re = 1568$, $E_0 = 3.6 \times 10^{-9}$.

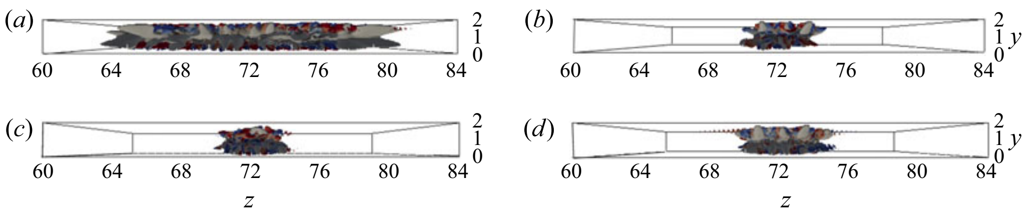

Figure 8. Minimal seeds at target time $t = T$ for different Reynolds numbers: isosurfaces of negative streamwise velocity ($u = -0.0025$, light grey) and Q-criterion ($Q = 0.003$) coloured by the streamwise vorticity (positive red, negative blue). Here: (*a*) $Re = 1000$, $E_0 = 5.5 \times 10^{-7}$; (*b*) $Re = 1150$, $E_0 = 4.7 \times 10^{-8}$; (*c*) $Re = 1250$, $E_0 = 2.9 \times 10^{-8}$; (*d*) $Re = 1568$, $E_0 = 3.6 \times 10^{-9}$.

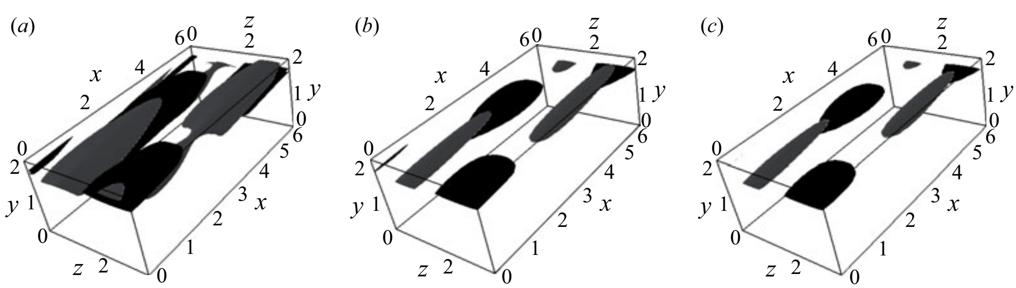

Figure 9. Minimal seeds for (*a*) $Re = 1400$, (*b*) $Re = 1568$, (*c*) $Re = 1650$; isosurfaces of the streamwise velocity (light grey for positive and black for negative values, $u = \pm 0.005$.

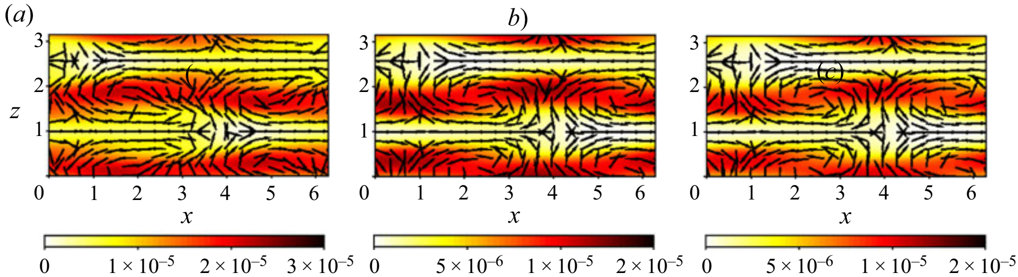

Figure 10. Isocontours of the crossflow energy E_{cf} with the normalized y-integrated large-scale flow (vectors) for the minimal seed in the small domain for (*a*) Re = 1400, (*b*) Re = 1568, and (*c*) Re = 1650.

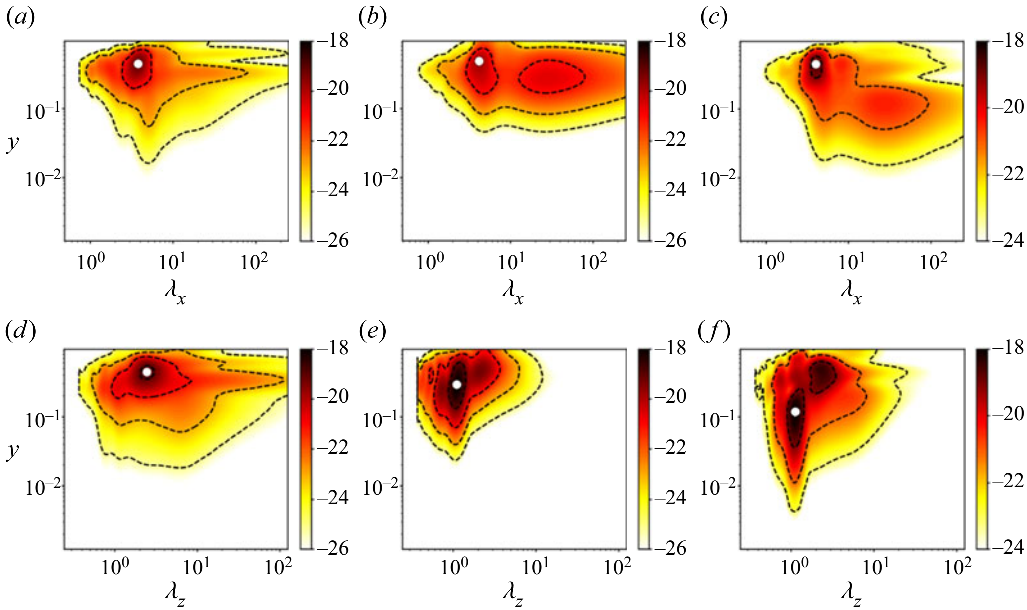

Figure 11. Logarithm of the premultiplied spectral energy versus the wall-normal distance y^+ for the initial optimal solution for $T = 100$, $Re = 1150$, with $E_0 = 1.1 \times 10^{-7}$, coloured contours, and $E_0 = 4.7 \times 10^{-8}$, black contours. The white dots indicate the energy peaks. Here: (*a*) $\lambda_x E_{uu}(\lambda_x)$. (*b*) $\lambda_x E_{vv}(\lambda_x)$, (*c*) $\lambda_x E_{ww}(\lambda_x)$, (*d*) $\lambda_z E_{uu}(\lambda_x)$, (*e*) $\lambda_z E_{vv}(\lambda_x)$, (*f*) $\lambda_z E_{ww}(\lambda_x)$.

Re	$(\lambda_x)_u$	$(\lambda_z)_u$	$(\lambda_x)_v$	$(\lambda_z)_v$	$(\lambda_x)_w$	$(\lambda_z)_w$
1000	4.897	2.117	4.995	1.049	4.995	2.080
1150	3.784	2.449	4.163	1.105	4.028	1.125
1250	1.287	2.153	24.98	1.049	4.625	1.105
1568	3.244	2.838	3.518	0.790	3.642	1.759

Table 1. Streamwise and spanwise wavelengths λ_x, λ_z associated with the primary peaks of the premultiplied energy spectra of u, v, w, shown in figure 12 for different Reynolds numbers.

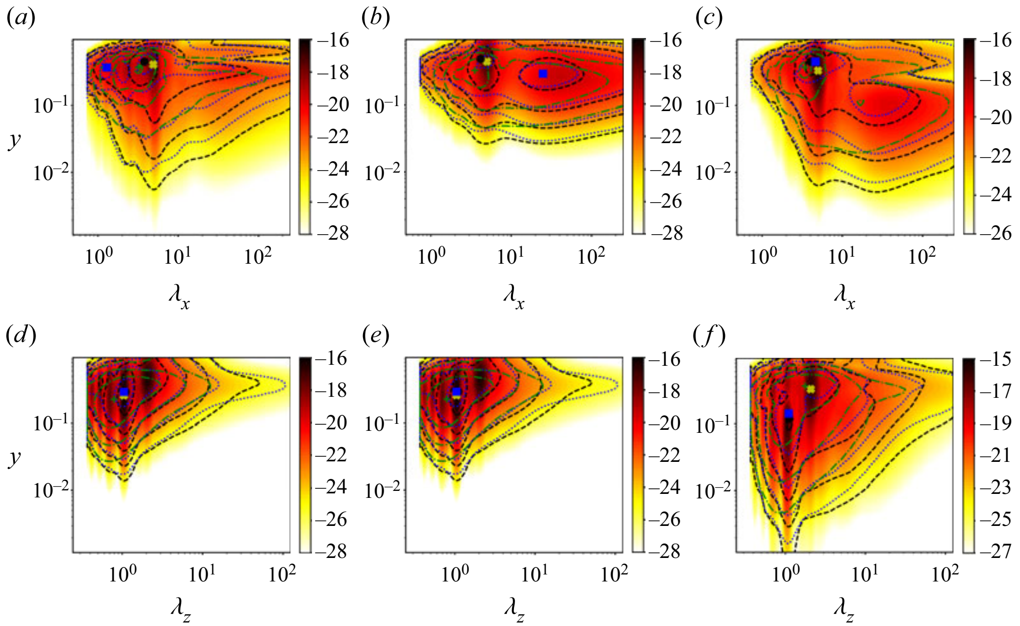

Figure 12. Logarithm of the premultiplied spectral energy versus the wall-normal distance y^+ for the initial optimal solution at different Reynolds numbers at $T = 100$: $Re = 1000$ for $E_0 = 5.5 \times 10^{-7}$ (coloured contours), $Re = 1150$ for $E_0 = 4.7 \times 10^{-8}$ (black contours), $Re = 1250$ for $E_0 = 2.9 \times 10^{-8}$ (blue contours), and $Re = 1568$ for $E_0 = 5.8 \times 10^{-9}$ (green contours). The symbols indicate the peaks of the energy, also reported in table 1. Here: (*a*) $\lambda_x E_{uu}(\lambda_x)$, (*b*) $\lambda_x E_{vv}(\lambda_x)$, (*c*) $\lambda_x E_{ww}(\lambda_x)$, (*d*) $\lambda_z E_{uu}(\lambda_z)$, (*e*) $\lambda_z E_{vv}(\lambda_z)$, (*f*) $\lambda_z E_{ww}(\lambda_z)$.

simulations initialized with the minimal seeds, is reported. In all cases, the kinetic energy increases strongly in time until saturating towards a statistically constant value. For the lowest considered Reynolds numbers, we observe a rapid initial increase of the kinetic energy, followed by a slow phase of saturation of the energy, whereas for larger *Re*, the initial growth is slower and leads to lower values of the kinetic energy at small time. One can notice once again that at $Re = 1000$, the flow appears to behave rather differently from what is observed at larger Reynolds numbers. However, the minimal seeds at larger *Re*, despite having lower initial energy, tend towards higher values of the kinetic energy at large times, suggesting that for larger Reynolds numbers, turbulence eventually occupies a larger portion of the domain.

This can be verified by analysing the time evolution of the crossflow energy and y-averaged flow fields for the minimal seeds at different Reynolds numbers. For $Re = 1150$, figure 14 shows that despite its quasi-symmetric initial shape (see figure 5), the localized minimal solution breaks its symmetry rapidly along the spanwise direction. A clearly asymmetric (but still spatially compact) structure can be seen already at $t = 500$, as shown in figure 14(*b*). Previous experimental and numerical works (Bullister & Orszag 1987) have observed that in their initial phases, spots are more unstable in their edges, so they rapidly incur symmetry breaking. Various authors (see, for instance, Lemoult *et al.* 2014) have related this symmetry-breaking phase to the development of sinuous instabilities of the streaks. This asymmetric wavepacket evolves via nucleation of new streaky structures (see Parente *et al.* (2021) concerning the mechanism of creation of the streaks) in the direction of the inclined laminar–turbulent interface, clearly forming

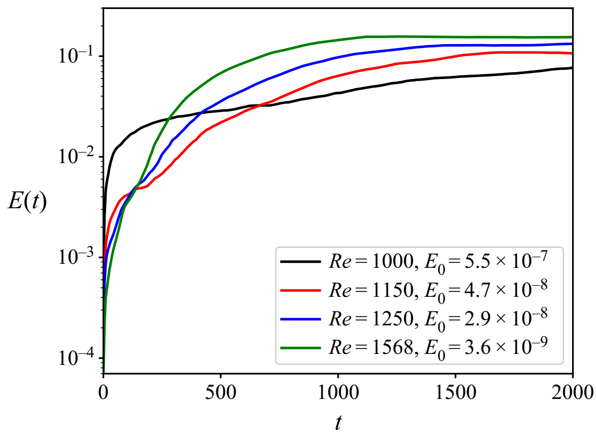

Figure 13. Time evolution of the kinetic energy for the minimal seeds obtained for the different considered Reynolds numbers.

a singular turbulent band, as can be observed for $t = 900$. The newly formed turbulent band continues growing in an oblique direction with angle $\approx 28^\circ$ until reaching the periodic boundaries, where it interacts with itself ($t = 1500$). This triggers splitting of the previously isolated band ($t = 2500$), which saturates, reaching a laminar–turbulent pattern filling the whole domain at $t = 4000$. The same behaviour has been observed by Tao & Xiong (2013) and Xiong *et al.* (2015) by injecting in a plane Poiseuille flow a 'seed' of the turbulent bands, similar in shape to the instantaneous field at $t = 500$ in figure 14. Analysing the large-scale flow, we can observe the formation of a small recirculation zone upstream of the spot during its evolution. Moreover, when the bands are formed, the large-scale flow is found to turn clockwise around bands with positive angle and anticlockwise around bands with negative angle. In fact, all the bands are formed in correspondence with the shear layer that divides the different vortices. A rather similar behaviour is observed at $Re = 1000$, as shown in figure 15. Despite that at small times ($t = 150$) the minimal seed evolves into a quasi-symmetric V-shaped spot, one of its two legs weakens in time ($t = 500$) and completely disappears at $t = 900$, evolving into a single band, as observed for $Re = 1150$. Whereas, looking at the evolution in time for the cases at higher Reynolds number, the flow presents the same behaviour observed experimentally and numerically when turbulence is triggered by a spot (Carlson *et al.* 1982; Alavyoon, Henningson & Alfredsson 1986; Henningson & Kim 1991; Aida *et al.* 2010, 2011). In fact, the localized perturbation initially evolves in the domain forming a turbulent spot, turning into a V-shape at $t = 500$, as shown in figure 16. At this time, two distinct fronts of the spots can be observed, which evolve in two symmetric bands with angle $\approx \pm 45^\circ$ growing obliquely in the domain, as shown at $t = 900$. At $t = 1200$, they start to interact with each other, forming a spatio-temporally complex final state composed of turbulent and laminar patterns ($t = 3000$). Qualitatively, the same behaviour is observed at $Re = 1568$, as shown in figure 17, although the spatial spreading of the bands appears to be more rapid than at lower Re, despite the initial energy of the perturbation being lower. Also in these cases, the bands are found to be generated right in the mixing layer between two large-scale counter-rotating vortices. Notice also that the same quasi-symmetric behaviour can be observed at lower Re, for a larger initial energy. In fact, the nonlinear optimal perturbation computed for $Re = 1150$ and $E_0 = 4.7 \times 10^{-8} > E_{0min}$ evolves in

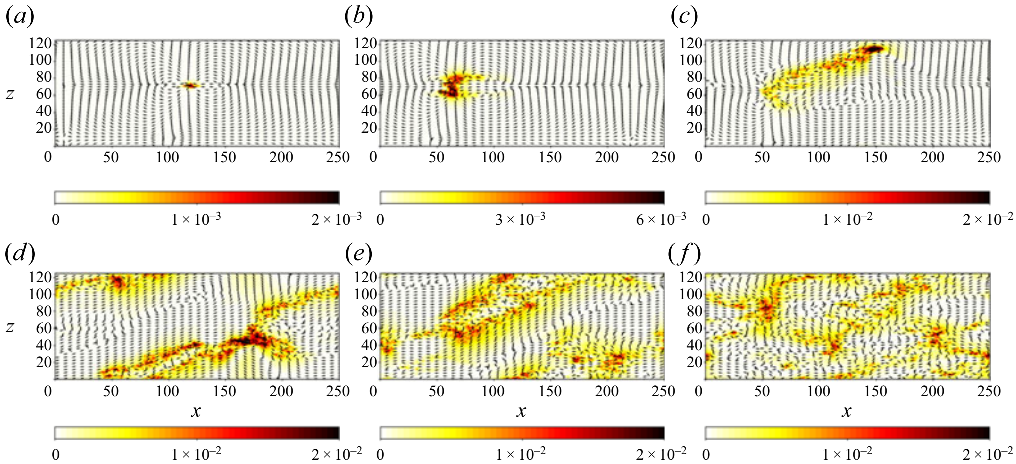

Figure 14. Isocontours of the crossflow energy E_{cf} together with the normalized y-integrated large-scale flow (vectors) for several instantaneous fields ($Re = 1150$, $E_0 = 4.7 \times 10^{-8}$, $T = 100$): (*a*) $t = 200$, (*b*) $t = 500$, (*c*) $t = 900$, (*d*) $t = 1500$, (*e*) $t = 2500$, (*f*) $t = 4000$.

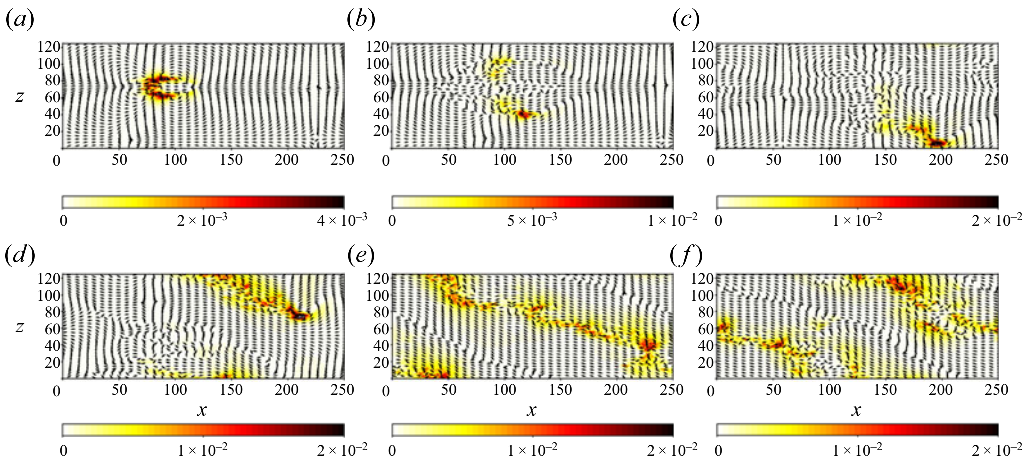

Figure 15. Isocontours of the crossflow energy E_{cf} together with the normalized y-integrated large-scale flow for several instantaneous fields ($Re = 1000$, $E_0 = 5.5 \times 10^{-7}$, $T = 100$): (*a*) $t = 150$, (*b*) $t = 500$, (*c*) $t = 900$, (*d*) $t = 1500$, (*e*) $t = 2500$, (*f*) $t = 3000$.

two distinct bands, showing a time evolution corresponding to that of the minimal seed at largest *Re* (not shown).

An explanation of this behaviour can be attempted by recalling that in the channel flow, turbulent stripes have a probability of decay that increases with time, and that decreases with the Reynolds number (Paranjape 2019). Thus since all minimal seeds present an almost spanwise-symmetric structure, two proto-bands begin to be created at the edges of the large-scale vortices characterizing the minimal seed. However, the probability of decay of these bands is higher for low Reynolds number, and increases in time, so when *Re* is sufficiently low, one of these bands dies out rapidly, leading to the development of one isolated band. Increasing *Re*, the probability of decay of an initial band is lower, while the probability of splitting increases. Thus both oblique bands originated at the sides of

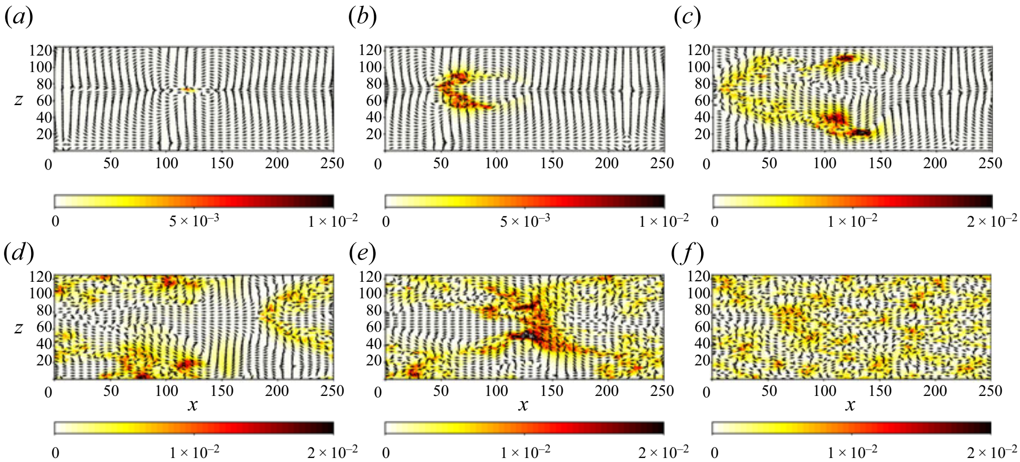

Figure 16. Isocontours of the crossflow energy E_{cf} together with the normalized y-integrated large-scale flow for several instantaneous fields ($Re = 1250$, $E_0 = 2.9 \times 10^{-8}$, $T = 100$): (*a*) $t = 200$, (*b*) $t = 500$, (*c*) $t = 900$, (*d*) $t = 1200$, (*e*) $t = 1500$, (*f*) $t = 3000$.

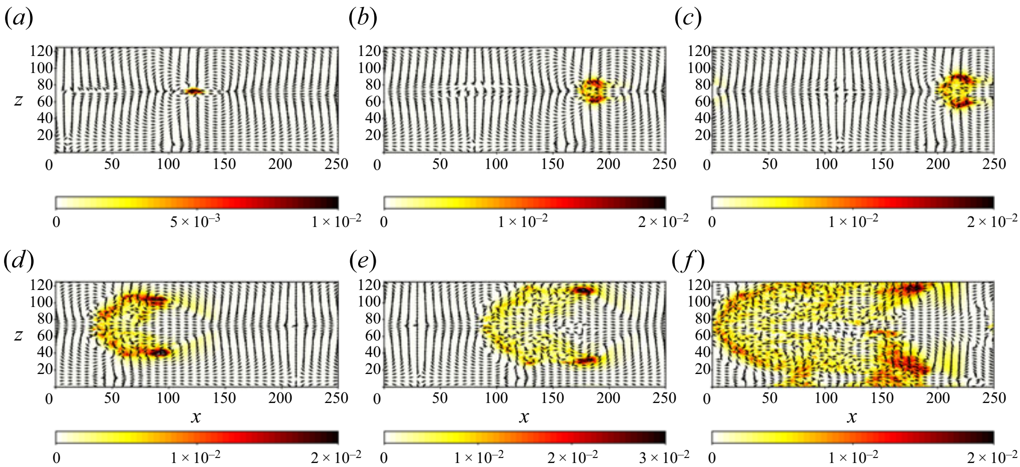

Figure 17. Isocontours of the crossflow energy E_{cf} together with the normalized y-integrated large-scale flow for several instantaneous fields ($Re = 1568$, $E_0 = 3.6 \times 10^{-9}$, $T = 150$): (*a*) $t = 200$, (*b*) $t = 300$, (*c*) $t = 350$, (*d*) $t = 500$, (*e*) $t = 600$, (*f*) $t = 900$.

the minimal seed survive longer in time, until they split and interact, leading rapidly to the establishment of a spatio-temporally complex final state. Notice that injecting more initial energy at low values of Re has the same effect as increasing Re. In fact, an optimal perturbation with $E_0 > E_{0min}$ is less spatially localized, and is able to reach a much larger kinetic energy at $T = 100$, leading to more spatially-extended and energetic proto-bands, which allows their sustainment for a longer time.

To corroborate this conjecture, we make use of the Reynolds–Orr equation to evaluate the production, P, and dissipation, ϵ, of kinetic energy as, respectively,

$$P = -u_i' u_j' \frac{\partial U_i}{\partial x_j}, \quad \epsilon = \frac{2}{Re} s_{ij}' s_{ij}', \quad \text{with } s_{ij}' = \frac{1}{2}\left(\frac{\partial u_i'}{\partial x_j} + \frac{\partial u_j'}{\partial x_i}\right), \tag{3.1}$$

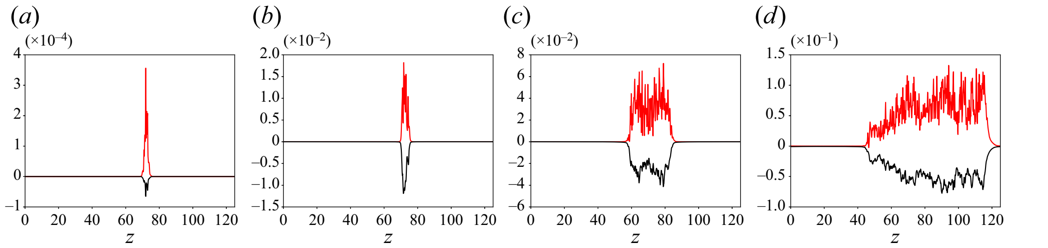

Figure 18. Spanwise distribution of the production (P, red line) and dissipation ($-\epsilon$, black line) terms integrated in x–y planes for different instantaneous fields obtained by evolving in time the minimal seed for $Re = 1150$, $E_0 = 4.7 \times 10^{-8}$, $T = 100$: (*a*) $t = 0$, (*b*) $t = 100$, (*c*) $t = 500$, (*d*) $t = 900$.

where the Einstein summation convention has been used. One can compare the time evolution of the production and dissipation terms, integrated in x–y planes, for the minimal seeds at $Re = 1150$ and $Re = 1250$, provided in figures 18 and 19. For both Reynolds numbers, at $t = 0$ the production presents one single peak almost in the centre of the spot ($z \approx 70$), which is found to exceed dissipation of almost an order of magnitude. Production of kinetic energy leads to a slight increase of the spanwise size of the wavepacket ($t = 100$), together with a further increase of the kinetic-energy production, probably due to the nucleation of new streaks that produce kinetic energy thanks to the lift-up effect. Due to the breakdown of the structures inside the spot, dissipation increases as well, reaching almost the same value of the production term. Notice also that a weak secondary peak begins to be visible in the production term. At $t = 500$, the spot has increased its size strongly in the spanwise direction, presenting a quasi-symmetric shape with two peaks at $z \approx 55$–60 and $z \approx 80$–85. However, at $t = 900$, the evolution of the production and dissipation terms begins to differ strongly between the two considered Reynolds numbers. For $Re = 1250$, the spanwise distribution of the dissipation and production terms remains quasi-spanwise-symmetric, centred at $z \approx 70$, with two distinct laminar–turbulent fronts at $z \approx 20$ and $z \approx 110$ (see figure 19). Whereas, for $Re = 1150$, the leftmost part of the packet has almost faded away, while the rightmost part has expanded up to $z \approx 110$, as shown in figure 18. The analysis of the production and dissipation terms indicates clearly that the minimal seed for turbulent bands leads to the generation of two almost symmetric regions of high production and dissipation, which can be seen as two distinct proto-bands. However, for lower Reynolds numbers, the weaker of these two proto-bands decays rapidly, leading to the development of an isolated band, whereas at larger Reynolds numbers, both bands survive for a sufficiently long amount of time to begin self-interacting.

4. Conclusion

In this work, we have investigated the minimal-energy perturbations for the generation of turbulent bands in plane Poiseuille flow. A nonlinear optimization maximizing the kinetic energy at a given target time, coupled with initial energy bisection, has been used. The optimization was performed in very large domains, for a range of Reynolds numbers for which turbulent bands are sustained and lead to a spatio-temporally complex turbulent–laminar final state, namely $Re = 1000, 1150, 1250, 1568$ (the lowest value being close to the threshold Re for which bands splitting and turbulence spreading can be observed). The influence of the Reynolds number on the minimal energy threshold for

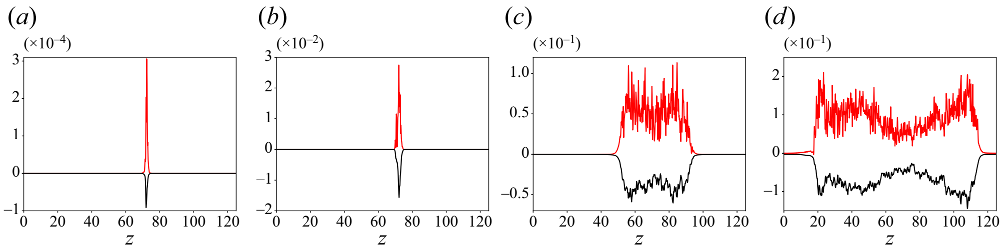

Figure 19. Spanwise distribution of the production (P, red line) and dissipation ($-\epsilon$, black line) terms integrated in x–y planes for different instantaneous fields obtained by evolving in time the minimal seed for $Re = 1250$, $E_0 = 2.9 \times 10^{-8}$, $T = 100$: (*a*) $t = 0$, (*b*) $t = 100$, (*c*) $t = 500$, (*d*) $t = 900$.

generating turbulent bands ($E_{0_{min}}$) is analysed. In accordance with previous work carried out on other shear flows in small domains, the minimal seed has been found to scale with Re following a power law $E_{0_{min}} \propto Re^{-\gamma}$, although a sufficiently good fit is found only by restraining the analysis to $Re > 1000$. However, the value of γ recovered in the present work ($\gamma \approx 8.5$) is approximately four times larger than the values reported in previous works ($\gamma \approx 2.7$ in Duguet *et al.* (2013), $\gamma \approx 2$ in Cherubini *et al.* (2015)). This may be due either to the different type of flow or to the very large domain size. Minimal seed computations carried out in a much smaller domain provided a scaling law very close to that found for the large one, although in a a limited range of Re very close to the threshold value for observing sustained turbulence. Whereas, restraining the range of Re to the largest values, the scaling appears to drop to -3.3, which is consistent with the values found for other shear flows. Moreover, the minimal energy threshold for transition to turbulence in the large domain is several orders of magnitude lower than that found for this smaller domain, and the structure of the minimal seeds changes as well.

For all values of the Reynolds numbers analysed, the minimal-energy perturbation able to generate turbulent bands is a spatially localized spot-like structure composed of finite-size streaks and elongated vortices. A more marked localization of the minimal seed is found when Re increases. As previously reported for the channel flow in the presence of spatially-localized spots, a large-scale flow having a quadrupolar structure has been found to surround the small-scale localized minimal perturbations. These minimal perturbations have dominant wavelengths $\approx$4 and $\approx$1 in the streamwise and spanwise directions, respectively. Nonlinear optimal perturbations, with energy higher than minimal, are characterized by similar shape and wavenumbers.

The evolution of the minimal seeds towards the turbulent bands has been investigated. For $Re < 1250$, the minimal seeds evolve in time creating an isolated oblique band, whereas for $Re \geqslant 1250$, it gives rise to two distinct bands that grow quasi-symmetrically in the spanwise direction. This quasi-symmetrical evolution is observed also at lower Re for non-minimal optimal perturbations. An analysis of the production and dissipation of kinetic energy integrated in the streamwise and wall-normal directions shows that in all cases, the initial spot-like perturbation evolves in a quasi-symmetric fashion, giving rise to two proto-bands at the edges of the large-scale flow characterizing the minimal seeds. However, since the probability of decay of the bands increases in time and is higher for low Reynolds number, when Re is sufficiently low, one of these bands rapidly dies out, leading to the development of one isolated band. Whereas, for larger values of Re, the probability of decay of an initial band is lower, while the probability of splitting increases.

Thus both oblique bands originated at the sides of the minimal seed survive for a longer time, until they split and interact, leading rapidly to the establishment of a spatio-temporally complex final state. Injecting more initial energy at low values of *Re* has the same effect as increasing *Re*, since a more spatially extended disturbance with higher kinetic energy is reached at a small time, leading to longer and more energetic proto-bands, able to be sustained for a longer time.

This work elucidates two (apparently distinct) minimal-energy mechanisms for the generation of turbulent bands in channel flow. It appears that both the initial and final states are very sensitive to the energy and Reynolds numbers characterizing the flow, highlighting the complexity of the laminar–turbulent patterned state and its initial seed. The selection of one of these two mechanisms appears to be affected by the probability of decay of the newly created stripe, which increases with time, but decreases with the Reynolds number. Future work will aim to extend the present investigation to other shear flows presenting spatially patterned turbulence.

Funding. This work was granted access to the HPC resources of IDRIS under the allocation 2020-A0072A06362 and A0092A06362 made by GENCI.

Declaration of interests. The authors report no conflict of interest.

Author ORCIDs.
E. Parente https://orcid.org/0000-0003-3978-4351;
J.-Ch. Robinet https://orcid.org/0000-0002-3529-6003;
P. De Palma https://orcid.org/0000-0002-7831-6115;
S. Cherubini https://orcid.org/0000-0003-4843-4927.

REFERENCES

AIDA, H., TSUKAHARA, T. & KAWAGUCHI, Y. 2010 DNS of turbulent spot developing into turbulent stripe in plane Poiseuille flow. In *Fluids Engineering Division Summer Meeting*, pp. 2125–2130. ASME Digital Collection.

AIDA, H., TSUKAHARA, T. & KAWAGUCHI, Y. 2011 Development of a turbulent spot into a stripe pattern in plane Poiseuille flow. arxiv:1410.0098.

ALAVYOON, F., HENNINGSON, D.S. & ALFREDSSON, P.H. 1986 Turbulent spots in plane Poiseuille flow visualization. *Phys. Fluids* **29** (4), 1328–1331.

AVILA, K., MOXEY, D., DE LOZAR, A., AVILA, M., BARKLEY, D. & HOF, B. 2011 The onset of turbulence in pipe flow. *Science* **333** (6039), 192–196.

BARKLEY, D. & TUCKERMAN, L.S. 2005 Computational study of turbulent laminar patterns in Couette flow. *Phys. Rev. Lett.* **94** (1), 014502.

BRAND, E. & GIBSON, J.F. 2014 A doubly localized equilibrium solution of plane Couette flow. *J. Fluid Mech.* **750**, R3.

BULLISTER, E.T. & ORSZAG, S.A. 1987 Numerical simulation of turbulent spots in channel and boundary layer flows. *J. Sci. Comput.* **2**, 263–281.

CARLSON, D.R., WIDNALL, S.E. & PEETERS, M.F. 1982 A flow-visualization study of transition in plane Poiseuille flow. *J. Fluid Mech.* **121**, 487–505.

CHANTRY, M., TUCKERMAN, L.S. & BARKLEY, D. 2016 Turbulent–laminar patterns in shear flows without walls. *J. Fluid. Mech.* **791**, R8.

CHERUBINI, S., DE PALMA, P. & ROBINET, J.-C. 2015 Nonlinear optimals in the asymptotic suction boundary layer: transition thresholds and symmetry breaking. *Phys. Fluids* **27** (3), 034108.

CHERUBINI, S., DE PALMA, P., ROBINET, J.-C.. & BOTTARO, A. 2010*a* Rapid path to transition via nonlinear localized optimal perturbations in a boundary-layer flow. *Phys. Rev.* E **82** (6), 066302.

CHERUBINI, S., DE PALMA, P., ROBINET, J.-C. & BOTTARO, A. 2011 The minimal seed of turbulent transition in the boundary layer. *J. Fluid Mech.* **689**, 221–253.

CHERUBINI, S., ROBINET, J.-C., BOTTARO, A. & DE PALMA, P. 2010*b* Optimal wave packets in a boundary layer and initial phases of a turbulent spot. *J. Fluid Mech.* **656**, 231–259.

COULIOU, M. & MONCHAUX, R. 2015 Large-scale flows in transitional plane Couette flow: a key ingredient of the spot growth mechanism. *Phys. Fluids* **27** (3), 034101.

DUGUET, Y., MONOKROUSOS, A., BRANDT, L. & HENNINGSON, D.S. 2013 Minimal transition thresholds in plane Couette flow. *Phys. Fluids* **25** (8), 084103.

DUGUET, Y. & SCHLATTER, P. 2013 Oblique laminar–turbulent interfaces in plane shear flows. *Phys. Rev. Lett.* **110**, 034502.

DUGUET, Y., SCHLATTER, P. & HENNINGSON, D.S. 2010 Formation of turbulent patterns near the onset of transition in plane Couette flow. *J. Fluid Mech.* **650**, 119–129.

ECKHARDT, B., SCHNEIDER, T.M., HOF, B. & WESTERWEEL, J. 2007 Turbulence transition in pipe flow. *Annu. Rev. Fluid Mech.* **39**, 447–468.

EMMONS, H.W. 1951 The laminar–turbulent transition in a boundary layer – Part I. *J. Aeronaut. Sci.* **18** (7), 490–498.

FARANO, M., CHERUBINI, S., ROBINET, J.-C. & DE PALMA, P. 2015 Hairpin-like optimal perturbations in plane Poiseuille flow. *J. Fluid Mech.* **775**, R2.

FARANO, M., CHERUBINI, S., ROBINET, J.-C. & DE PALMA, P. 2016 Subcritical transition scenarios via linear and nonlinear localized optimal perturbations in plane Poiseuille flow. *Fluid Dyn. Res.* **48** (6), 061409.

FARANO, M., CHERUBINI, S., ROBINET, J.-C. & DE PALMA, P. 2017 Optimal bursts in turbulent channel flow. *J. Fluid Mech.* **817**, 35–60.

FOURES, D.P.G., CAULFIELD, C.P. & SCHMID, P.J. 2013 Localization of flow structures using ∞-norm optimization. *J. Fluid Mech.* **729**, 672–701.

GIBSON, J.F., *et al.* 2021 Channelflow 2.0. channelflow.ch.

GOMÉ, S., TUCKERMAN, L.S. & BARKLEY, D. 2020 Statistical transition to turbulence in plane channel flow. *Phys. Rev. Fluids* **5**, 083905.

GRIEWANK, A. & WALTHER, A. 2000 Algorithm 799: revolve: an implementation of checkpointing for the reverse or adjoint mode of computational differentiation. *ACM Trans. Math. Softw.* **26** (1), 19–45.

HENNINGSON, D.S. & KIM, J. 1991 On turbulent spots in plane Poiseuille flow. *J. Fluid Mech.* **228**, 183–205.

HINZE, M., WALTHER, A. & STERNBERG, J. 2006 An optimal memory-reduced procedure for calculating adjoints of the instationary Navier–Stokes equations. *Opt. Control Applics. Meth.* **27** (1), 19–40.

JIMÉNEZ, J. 2013 How linear is wall-bounded turbulence? *Phys. Fluids* **25** (11), 110814.

KASHYAP, P.V., DUGUET, Y. & DAUCHOT, O. 2020 Flow statistics in the transitional regime of plane channel flow. *Entropy* **22** (9), 1001.

KERSWELL, R.R. 2018 Nonlinear nonmodal stability theory. *Annu. Rev. Fluid Mech.* **50** (1), 319–345.

KERSWELL, R.R., PRINGLE, C.C.T. & WILLIS, A.P. 2014 An optimisation approach for analysing nonlinear stability with transition to turbulence in fluids as an exemplar . *Rep. Prog. Phys.* **77**, 085901.

KLINGMANN, B.G.B. 1992 On transition due to three-dimensional disturbances in plane Poiseuille flow. *J. Fluid Mech.* **240**, 167–195.

KLOTZ, L., PAVLENKO, A.M. & WESFREID, J.E. 2021 Experimental measurements in plane Couette–Poiseuille flow: dynamics of the large- and small-scale flow. *J. Fluid Mech.* **912**, A24.

LAGHA, M. & MANNEVILLE, P. 2007 Modeling of plane Couette flow. I. Large scale flow around turbulent spots. *Phys. Fluids* **19** (9), 094105.

LEMOULT, G., AIDER, J.-L. & WESFREID, J.E. 2013 Turbulent spots in a channel: large-scale flow and self-sustainability. *J. Fluid Mech.* **731**, R1.

LEMOULT, G., GUMOWSKI, K., AIDER, J.-L. & WESFREID, J.E. 2014 Turbulent spots in channel flow: an experimental study. *Eur. Phys. J.* E **37** (4), 1–11.

LUNDBLADH, A. & JOHANSSON, A.V. 1991 Direct simulation of turbulent spots in plane Couette flow. *J. Fluid Mech.* **229**, 499–516.

MARENSI, E., WILLIS, A.P. & KERSWELL, R.R. 2019 Stabilisation and drag reduction of pipe flows by flattening the base profile. *J. Fluid Mech.* **863**, 850–875.

MARXEN, O. & ZAKI, T.A. 2019 Turbulence in intermittent transitional boundary layers and in turbulence spots. *J. Fluid Mech.* **860**, 350–383.

MONOKROUSOS, A., BOTTARO, A., BRANDT, L., DI VITA, A. & HENNINGSON, D.S. 2011 Nonequilibrium thermodynamics and the optimal path to turbulence in shear flows. *Phys. Rev. Lett.* **106** (13), 134502.

ORR, W.M'F. 1907 The stability or instability of the steady motions of a perfect liquid and of a viscous liquid. Part II: a viscous liquid. In *Proceedings of the Royal Irish Academy. Section A: Mathematical and Physical Sciences*, pp. 69–138. JSTOR.

PARANJAPE, C. 2019 Onset of turbulence in plane Poiseuille flow. PhD thesis, IST Austria.

PARENTE, E., ROBINET, J.-C., DE PALMA, P. & CHERUBINI, S. 2021 Linear and nonlinear optimal growth mechanisms for generating turbulent bands. *J. Fluid Mech.* **938**, A25.

PRIGENT, A., GRÉGOIRE, G., CHATÉ, H., DAUCHOT, O. & VAN SAARLOOS, W. 2002 Large-scale finite-wavelength modulation within turbulent shear flows. *Phys. Rev. Lett.* **89** (1), 014501.

PRINGLE, C.C.T. & KERSWELL, R.R. 2010 Using nonlinear transient growth to construct the minimal seed for shear flow turbulence. *Phys. Rev. Lett.* **105** (15), 154502.

PRINGLE, C.C.T., WILLIS, A.P. & KERSWELL, R.R. 2012 Minimal seeds for shear flow turbulence: using nonlinear transient growth to touch the edge of chaos. *J. Fluid Mech.* **702**, 415–443.

PRINGLE, C.C.T., WILLIS, A.P. & KERSWELL, R.R. 2015 Fully localised nonlinear energy growth optimals in pipe flow. *Phys. Fluids* **27** (6), 064102.

RABIN, S.M.E., CAULFIELD, C.P. & KERSWELL, R.R. 2012 Triggering turbulence efficiently in plane Couette flow. *J. Fluid Mech.* **712**, 244–272.

RABIN, S.M.E., CAULFIELD, C.P. & KERSWELL, R.R. 2014 Designing a more nonlinearly stable laminar flow via boundary manipulation. *J. Fluid Mech.* **738**, R1.

REYNOLDS, O. 1883 III. An experimental investigation of the circumstances which determine whether the motion of water shall be direct or sinuous, and of the law of resistance in parallel channels. *Proc. R. Soc. Lond.* **35** (224–226), 84–99.

SCHUMACHER, J. & ECKHARDT, B. 2001 Evolution of turbulent spots in a parallel shear flow. *Phys. Rev.* E **63** (4), 046307.

SHIMIZU, M. & MANNEVILLE, P. 2019 Bifurcations to turbulence in transitional channel flow. *Phys. Rev. Fluids* **4** (11), 113903.

SONG, B. & XIAO, X. 2020 Trigger turbulent bands directly at low Reynolds numbers in channel flow using a moving-force technique. *J. Fluid Mech.* **903**, A43.

TAO, J.J., ECKHARDT, B. & XIONG, X.M. 2018 Extended localized structures and the onset of turbulence in channel flow. *Phys. Rev. Fluids* **3** (1), 011902.

TAO, J. & XIONG, X. 2013 The unified transition stages in linearly stable shear flows. In *Fourteenth Asia Congress of Fluid Mechanics, Hanoi and Halong, 15–19 October*.

TAO, J. & XIONG, X. 2017 The unified transition stages in linearly stable shear flows. arXiv:1710.02258.

TSUKAHARA, T., KAWAGUCHI, Y. & KAWAMURA, H. 2014 An experimental study on turbulent-stripe structure in transitional channel flow. In *Proceedings of the Sixth International Symposium on turbulence heat and mass transfer*. Begell House.

TSUKAHARA, T., SEKI, Y., KAWAMURA, H. & TOCHIO, D. 2005 DNS of turbulent channel flow at very low Reynolds numbers. In *Fourth International Symposium on Turbulence and Shear Flow Phenomena*. Begel House Inc.

TUCKERMAN, L.S. & BARKLEY, D. 2011 Patterns and dynamics in transitional plane Couette flow. *Phys. Fluids* **23** (4), 041301.

TUCKERMAN, L.S., CHANTRY, M. & BARKLEY, D. 2020 Patterns in wall-bounded shear flows. *Annu. Rev. Fluid Mech.* **52**, 343–367.

TUCKERMAN, L.S., KREILOS, T., SCHROBSDORFF, H., SCHNEIDER, T.M. & GIBSON, J.F. 2014 Turbulent–laminar patterns in plane Poiseuille flow. *Phys. Fluids* **26** (11), 114103.

VAVALIARIS, C., BENEITEZ, M. & HENNINGSON, D.S. 2020 Optimal perturbations and transition energy thresholds in boundary layer shear flows. *Phys. Rev. Fluids* **5** (6), 062401.

WANG, Z., GUET, C., MONCHAUX, R., DUGUET, Y. & ECKHARDT, B. 2020 Quadrupolar flows around spots in internal shear flows. *J. Fluid Mech.* **892**, A27.

XIAO, X. & SONG, B. 2020 The growth mechanism of turbulent bands in channel flow at low Reynolds numbers. *J. Fluid Mech.* **883**, R1.

XIONG, X., TAO, J., CHEN, S. & BRANDT, L. 2015 Turbulent bands in plane-Poiseuille flow at moderate Reynolds numbers. *Phys. Fluids* **27** (4), 041702.

ZUCCHER, S., LUCHINI, P. & BOTTARO, A. 2004 Algebraic growth in a Blasius boundary layer: optimal and robust control by mean suction in the nonlinear regime. *J. Fluid Mech.* **513**, 135–160.